Inorganic Chemistry
Article
pubs.acs.org/IC

On the Anomalous Magnetic Behavior and the Multiferroic Properties in $BiMn_2O_5$

Q. Liu,[†,‡,§] D. Sallagoity,[†,‡] M. Josse,[†,‡] and O. Toulemonde*[,†,‡]

[†]CNRS, ICMCB, UPR 9048, F-33600 Pessac, France
[‡]Université Bordeaux, ICMCB, UPR 9048, F-33600 Pessac, France
[§]Max-Planck Institute for Chemical Physics of Solids, Nöthnitzer Strasse 40, D-01187 Dresden, Germany

S *Supporting Information*

ABSTRACT: Sealed-tube synthesis of $BiMn_2O_5$ materials and their physical properties have rationally been reinvestigated depending on the reactants. The aim of the study was to characterize its potential multiferroic properties and to investigate the anomalous magnetic properties in relation to the expected ferroelectric properties. Rietveld refinement of the room temperature X-ray diffraction data shows the stability of the crystallographic structure with a Mn^{3+}/Mn^{4+} ratio far from 1 because of bismuth and oxygen deficiencies despite the sealed-tube synthesis. Our detailed magnetic susceptibility and specific heat data analysis unambiguously support an intrinsic anomalous magnetic behavior in relation to the establishment of a magnetic short-range ordering far from the Néel temperature. Around room temperature, oxygen vacancies are responsible for supporting the dielectric loss peak measured, and, interestingly, the so-called *T**, which was underlined in relation to an anomalous phonon shift (García-Flores, A. F.; et al. *Phys. Rev. B* **2006**, *73*, 104411), is not a characteristic temperature in relation to the multiferroic properties because no ferroelectric transition was detected.

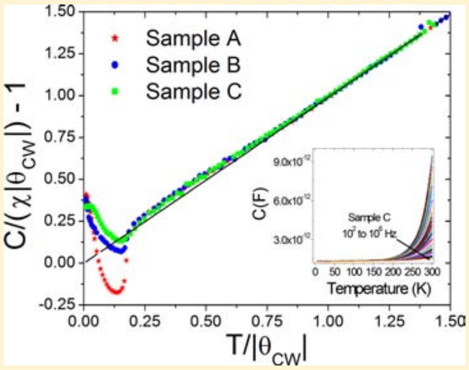

INTRODUCTION

Smart materials are sensitive to external stimuli such as stress, temperature, and an electric or magnetic field. Thus, several technological inputs are expected. Multiferroic materials belong to these kinds of smart materials when their ferroelectric properties can be tuned by applying a magnetic field, indicating that an effective magnetoelectric coupling exists.[1] Recently, two novel classes of multiferroic materials have emerged in which ferroelectricity can be triggered by either magnetic ordering[2] or charge ordering.[3] Tremendous work is devoted to these novel classes of materials, and isostructural RMn_2O_5 (R = rare earth, Y or Bi) insulators[4] are typical examples.

The RMn_2O_5 oxides were first described in the 1960s by Quezel-Ambrunaz et al.[5] and Bertaut et al.[6] following single-crystal growth by a Bi_2O_3 flux method. Later on, the RMn_2O_5 class of materials was pointed out to be fundamentally relevant to a charge-ordering phenomenon in relation to the existence of two crystallographically independent sites for Mn atoms.[7] The proposed crystallographic framework is built up of $[Mn^{4+}O_6]$ octahedra sharing edges, forming an infinite linear chain along the *c* axis, and interconnected with $[Mn^{3+}O_5]$ square pyramids. Aiming to induce novel physical properties, B-site substitution of RMn_2O_5 by Fe was carried out.[8] For the substitution ratio Mn/Fe = 1, high-resolution neutron powder X-ray diffraction (XRD) suggested that Fe^{3+} and Mn^{4+} ions were ordered in square-pyramidal and octahedral sites, respectively.[9] This proposed charge-ordering model is in contrast with previous single-crystal XRD analysis in $BiFeMnO_5$ material,[10] where it was claimed that Fe^{3+} ions were only located on octahedral sites. Meanwhile, Nguyen and co-workers reported that the crystallographic phases of $BiMn_{2-x}B_xO_5$ ($0 \leq x \leq 0.5$; B = Fe, Al, and Ti) were stable even if the Mn^{3+}/Mn^{4+} ratio was not equal to 1 with a slight increase of the cell parameters with *x*.[11]

Regarding the magnetic properties, $BiMn_2O_5$ exhibits a commensurate magnetic structure in contrast with the incommensurate magnetic structure observed for $LnMn_2O_5$ (Ln = lanthanide).[12] Even if a magnetic transition from the paramagnetic-to-antiferromagnetic state was often observed when the temperature decreases, a low-temperature ferrimagnetic state has also been shown.[13,14] Indeed, more divergences are also observed (i) on the transport properties when Alonso and co-workers[7] pointed out that their materials were insulating with $\rho > 10^8 \Omega\cdot$cm at room temperature in contrast with Lin and co-workers finding that the high-temperature conductivity of their phase is thermally activated (E_A= 0.38 eV within the 200−450 K range)[15] and (ii) on the dielectric response when Lin and co-workers highlight similarities between the activation energies from the dielectric relaxation and that from the high-temperature conductivity to finally conclude that $BiMn_2O_5$ is not relaxor ferroelectric, contrary to the conclusion of Fier and co-workers.[16] It is likely that these discrepancies are due to the large number of chemistry methods used to synthesize the

Received: December 20, 2012
Published: July 1, 2013

oxide and certainly a lack of discussion about the actual stoichiometry of the sample.

Taking into account all of these works, our aim is to discuss the magnetic and dielectric properties of $BiMn_2O_5$ depending on the chemical precursors and/or the sintering process used for the synthesis. Especially, we focus our study on the occurrence (or not) of an anomalous magnetic behavior that would be in relation to dielectric anomalies.[16] This paper is organized as follows. In the first section, X-ray crystallographic analysis at room temperature confirms the bismuth deficiency shown by inductively coupled plasma (ICP) analysis despite the sealed-tube synthesis. Then, we carefully describe in the second section the magnetic properties in relation to this bismuth deficiency. In the third section, specific heat measurements and dielectric properties are presented. Finally, despite the lack of multiferroic properties, we pointed out that the anomalous magnetic properties are intrinsic.

■ EXPERIMENTAL SECTION

Synthesis. All polycrystalline samples of nominal composition $BiMn_2O_5$ were synthesized by a standard solid-state reaction method starting with the reagent Bi_2O_3, Mn_2O_3, and MnO_2 with purity above 99.9%. The Bi_2O_3 powder was first heated up at 300 °C for 12 h to avoid hydrate and CO_2 adsorption. The starting precursors (Bi_2O_3 + Mn_2O_3 + $2MnO_2$ for samples A and B, Bi_2O_3 + $4MnO_2$ for sample C, and $1.025Bi_2O_3$ + Mn_2O_3 + $2MnO_2$ for sample D) were mixed, homogenized, and placed in evacuated a silica tube to limit the bismuth loss through volatilization. Sample A was kept as powder, whereas samples B and C were pressed into pellets. Following numerous tests, the selected thermal treatment was defined in which the samples are heated at 850 °C, just above the melting point 824 °C of Bi_2O_3, for 24 h and then cooled to room temperature with a rate of 30 °C/h.

Powder XRD. Powder XRD patterns at room temperature were collected with a Cu $K\alpha_1$(1.5406 Å) radiation source in PANalytical X'Pert Pro apparatus. All of the data were collected from 5° to 120° in steps of 0.08° on a continuous-mode scan with a counting time of 60 s/step for advanced structural investigations. All of the diffraction patterns have been refined with the Rietveld refinement method[17] using *FULLPROF* program package. The background was fitted with a 12-coefficient polynomial function, and the peak shapes were simulated by a Thompson−Cox−Hastings pseudo-Voigt function. During the refinement, the scale factor, background coefficient, zero-point, microstrain and microsize effects, unit cell parameters, atomic positions, bismuth occupancies, Debye Weller factors, and asymmetry were refined. Unique isotropic atomic displacement parameters were used for all oxygen positions in all refinements.

Chemical Analysis. The expected cationic chemical composition was confirmed by optical emission spectroscopy excited with inductively coupled plasma optical emission spectroscopy (ICP-OES). The oxygen content was deduced from the oxidation state of the transition elements. Besides, the oxygen contents were calculated by Mohr's salt titration with a standard potassium dichromate (0.1 N).[18]

Physical Properties. Direct-current (dc) magnetic susceptibility measurements were performed over the temperature range 2−300 K, using a Quantum Design XL-MPMS Squid magnetometer in zero-field-cooling (ZFC) and field-cooling (FC) conditions. The sample was introduced at room temperature and cooled in zero field at 5 K/min before the magnetic field was applied to reach 0.1 T. Specific heat measurements were performed using a Quantum Design Physical Properties Measurement System (PPMS). The alternating-current dielectric properties were measured using an HP4194a impedance bridge. The sample, after deposition of silver paste electrodes and attachment of tungsten wires for the sake of electrical connection, was placed in a Quantum Design PPMS. The dielectric measurements were carried out in the frequency range of 10^2−10^6 Hz (with the amplitude of the applied electric field being 1 V), at a heating rate of 1 K/min.

■ RESULTS

Figure 1 shows the powder XRD patterns of samples A−C collected at room temperature. Within the precision of our experiment, all of the phases show similar diffraction patterns and no impurity phases were detected. The crystal structures were refined with the *Pbam* space group using the initial structure model given by Alonso and co-workers.[7] The diffraction patterns, calculated fits, and difference curves are shown on the Supporting Information. Tables 1 and 2 list the characteristic parameters after the refinements and relevant atomic distances with respect to the literature, respectively. We fixed the manganese and oxygen occupancies (i.e., 2 Mn and 5 O atoms per formula unit) and successively refined the occupancy of bismuth in order to consider the bismuth deficiency in comparison to ICP-OES analysis, which is summed up in Table 3. The bismuth deficiency was already pointed out on samples prepared by solid-state reaction for which a bismuth deficiency might be expected.[19] It cannot be avoided even if the synthesis is performed using an excess of Bi_2O_3, as highlighted by the sample D study that was made on purpose with a molar excess of 2.5% for Bi_2O_3 within the sealed tube to compensate for bismuth volatilization regarding the molar bismuth deficiency found. The XRD pattern of sample D is not single phase because the main peak of the Bi_2O_3 phase is observed, as shown on the Supporting Information, and the result of the Rietveld refinement shows that the bismuth occupancy is on the same order of magnitude as those shown by samples A−C, suggesting that the bismuth deficiency is intrinsic on $BiMn_2O_5$.

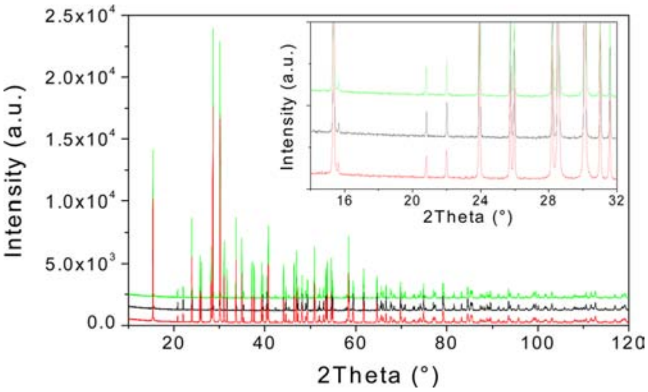

Figure 1. Room temperature XRD patterns of samples A−C from bottom to top. The inset shows a shorter angular range highlighting no extra peaks due to secondary phases. The patterns were equally vertically translated for better visualization.

We calculate and report in Table 2 and Figure 2 the mean-square relative deviations from the average bond length[21] to estimate the distortion of the three different $[Mn(1)O_6]$, $[Mn(2)O_5]$, and $[BiO_8]$ units considered as blocks to build up the crystallographic framework of $BiMn_2O_5$. They are defined by the equation

$$\Delta = \frac{1}{n}\sum_{n=1}^{n=i}\left(\frac{dMO_i - \langle dMO\rangle}{\langle dMO\rangle}\right)^2 \quad (1)$$

Table 1. Cell Parameters, Structural Parameters, and Relative Cationic Occupancies Obtained after the Rietveld Refinement for the Three Samples A (Top), B (Middle), and C (Bottom) Using *Pbam* Space Group

atom	position	x/a	y/b	z/c	B_{iso} (Å^2)	occupancy
Bi	4g	0.15949(5)	0.16549(4)	0.00000	0.136(13)	0.968(2)
Mn(1)	4f	0.00000	0.50000	0.2597(2)	0.123(32)	1
Mn(2)	4h	0.4067(1)	0.3503(1)	0.50000	0.303(35)	1
O(1)	4e	0.00000	0.00000	0.2857(8)	0.391(59)	1
O(2)	4g	0.1527(7)	0.4425(5)	0.00000	0.391(59)	1
O(3)	4h	0.1399(7)	0.4244(5)	0.50000	0.391(59)	1
O(4)	8i	0.3859(4)	0.1970(4)	0.2538(5)	0.391(59)	1
cell parameters a = 7.5641(1) Å, b = 8.5336(1) Å, c = 5.7616(1) Å						
R_{Bragg} = 1.90/R_f = 1.64/χ = 1.45						
atom	position	x/a	y/b	z/c	B_{iso} (Å^2)	occupancy
Bi	4g	0.15932(5)	0.16544(5)	0.00000	0.214(8)	0.942(2)
Mn(1)	4f	0.00000	0.50000	0.2615(2)	0.401(39)	1
Mn(2)	4h	0.4065(1)	0.3503(2)	0.50000	0.656(41)	1
O(1)	4e	0.00000	0.00000	0.2867(9)	0.546(67)	1
O(2)	4g	0.1493(7)	0.4431(6)	0.00000	0.546(67)	1
O(3)	4h	0.1414(7)	0.4238(5)	0.50000	0.546(67)	1
O(4)	8i	0.3873(4)	0.1985(4)	0.2556(5)	0.546(67)	1
cell parameters a = 7.5615(1) Å, b = 8.5346(1) Å, c = 5.7617(1) Å						
R_{Bragg} = 2.50/R_f = 2.07/χ = 1.72						
atom	position	x/a	y/b	z/c	B_{iso} (Å^2)	occupancy
Bi	4g	0.15951(4)	0.16541(4)	0.00000	0.430(12)	0.958(2)
Mn(1)	4f	0.00000	0.50000	0.2607(2)	0.511(30)	1
Mn(2)	4h	0.4067(1)	0.3504(1)	0.50000	0.766(34)	1
O(1)	4e	0.00000	0.00000	0.2878(7)	0.712(54)	1
O(2)	4g	0.1499(6)	0.4441(5)	0.00000	0.712(54)	1
O(3)	4h	0.1420(6)	0.4252(4)	0.50000	0.712(54)	1
O(4)	8i	0.3859(4)	0.1982(3)	0.2553(4)	0.712(54)	1
cell parameters a = 7.5658(1) Å, b = 8.5315(1) Å, c = 5.7615(1) Å						
R_{Bragg} = 1.99/R_f = 1.75/χ = 1.11						

with M = metal and n the number of metal−oxygen bonding within the unit. Interestingly, whatever the synthesis method used [citrate technique and subsequent treatment in air,[12] crystal growth by the flux method,[20] solid-state route using a sealed tube[11] (and our work), or solid-state route[19]] and whatever the type of diffraction performed to characterize the materials (from X-ray Lab beam[11] (and our work), from X-ray Synchrotron beam,[19,20] or from Neutron beam[12]), all of the mean-square relative deviations in relation to the average distortions are consistent. The only divergence is shown in the calculation using the data of ref 20 (sample 7 on Figure 2) for which no Bi−O bonding analysis is given. One can also notice that the distortion of the [Mn(2)O_5] units is on the same order of magnitude as the one of the [BiO_8] units and that they are both 1 order of magnitude higher than the average distortion of the [Mn(1)O_6] units.

Despite of the sealed-tube chemical synthesis, we could not avoid bismuth deficiency. However, our X-ray pattern analysis still suggests that the crystallographic phase is stable even if the Mn^{3+}/Mn^{4+} ratio is not equal to 1. Indeed, considering the bismuth deficiency shown in the ICP-OES analysis, our Mohr salt titration gives a high Mn^{3+}/Mn^{4+} ratio close to 2 with a slight difference between samples B (Mn^{3+} = 1.28 and Mn^{4+} = 0.72) and C (Mn^{3+} = 1.32 and Mn^{4+} = 0.68). Because the major error on the titration results is in the molar mass calculation that is highly influenced by the bismuth deficiency, one consequently estimates the same oxygen deficiency δ equal to 0.23 ± 0.02 for the both samples B and C. Such under-stoichiometry is interesting because it is somewhat in contrast with the ones of Alonso et al.[7] on RMn_2O_5 and with some others on the perovskite-type structure RMnO_3 (R = lanthanide)[22,23] for which the lanthanide deficiency is the result of an oxygen overstoichiometry, leading to an increase of the Mn^{4+} content. Regardless of the variable manganese and bismuth reactants and the sealed-tube synthesis, one can then unambiguously point out that our Bi^{3+} deficiency is due to bismuth volatilization.

In order to check the preparation effects on the magnetic behavior, the magnetic susceptibilities of the three single-phase samples have been measured and are shown in Figure 3. As the temperature decreases, an upturn around 40 K is shown on the magnetic susceptibility curves before a maximum revealing a magnetic transition (Figure 3a) is exhibited. Such a temperature dependence suggests the occurrence of antiferromagnetic ordering with a Néel temperature T_N. As shown in Table 4, T_N is shifted to lower temperature from sample C to sample A in relation to enhancement of the thermal hysteresis and abruptness of the transition. Interestingly, the magnitudes of these maxima in the magnetic susceptibility curves display the same order of magnitude as the ones shown by Munoz and co-workers[12] or Granado and co-workers[19] but are in contrast with the values reached when a ferrimagnetic behavior is revealed.[13,14]

On the inverse magnetic susceptibility versus temperature curves (Figure 3b), a relatively large range of temperatures is available to perform Curie−Weiss analysis ($1/\chi = T/C - \theta_{CW}/C$) for the three samples. It allows us to determine the Curie−Weiss temperature θ_{CW} and the Curie constant C, as listed in

Table 2. Selected Interatomic Distances, BVS Calculation, and the Relevant Distortion of the $[Mn(1)O_6]$, $[Mn(2)O_5]$, and $[BiO_8]$ Units from Equation 1 in Comparison with the Literature

$[Mn(1)O_6]$		$[Mn(2)O_5]$		$[RO_8]$		ref
Mn(1)−O(2) (×2)	1.953(4) Å	Mn(2)−O(1) (×2)	1.911(4) Å	Bi−O(1) (×2)	2.482(3) Å	our study, sample A
Mn(1)−O(3) (×2)	1.858(3) Å	Mn(2)−O(3)	2.114(5) Å	Bi−O(2)	2.364(5)Å	
Mn(1)−O(4) (×2)	1.890(3) Å	Mn(2)−O(4) (×2)	1.935(4) Å	Bi−O(2)	2.375(5)Å	
				Bi−O(4) (×2)	2.269(4) Å	
				Bi−O(4) (×2)	2.792(4) Å	
⟨Mn(1)−O⟩	1.900(3) Å	⟨Mn(2)−O⟩	1.961(4) Å	⟨Bi−O⟩	2.478(5) Å	
Δ	4.3×10^{-4}	Δ	15.5×10^{-4}	Δ	13.7×10^{-4}	
BVS	4.05(5)	BVS	2.96(5)	BVS	3.20(0)	
Mn(1)−O(2) (×2)	1.945(4) Å	Mn(2)−O(1) (×2)	1.908(4) Å	Bi−O(1) (×2)	2.485(4) Å	our study, sample B
Mn(1)−O(3) (×2)	1.859(4) Å	Mn(2)−O(3)	2.100(6) Å	Bi−O(2)	2.372(5) Å	
Mn(1)−O(4) (×2)	1.897(3) Å	Mn(2)−O(4) (×2)	1.918(4) Å	Bi−O(2)	2.385(5) Å	
				Bi−O(4) (×2)	2.286(4) Å	
				Bi−O(4) (×2)	2.783(4) Å	
⟨Mn(1)−O⟩	1.900(3) Å	⟨Mn(2)−O⟩	1.950(1) Å	⟨Bi−O⟩	2.483(4) Å	
Δ	3.43×10^{-4}	Δ	14.8×10^{-4}	Δ	12.3×10^{-4}	
BVS	4.05(1)	BVS	3.04(1)	BVS	3.12(7)	
Mn(1)−O(2) (×2)	1.942(3) Å	Mn(2)−O(1) (×2)	1.902(3) Å	Bi−O(1) (×2)	2.490(3) Å	our study, sample C
Mn(1)−O(3) (×2)	1.861(3) Å	Mn(2)−O(3)	2.102(5) Å	Bi−O(2)	2.380(4) Å	
Mn(1)−O(4) (×2)	1.898(3) Å	Mn(2)−O(4) (×2)	1.923(3) Å	Bi−O(2)	2.375(5) Å	
				Bi−O(4) (×2)	2.276(3) Å	
				Bi−O(4) (×2)	2.793(3) Å	
⟨Mn(1)−O⟩	1.900(3) Å	⟨Mn(2)−O⟩	1.940(1) Å	⟨Bi−O⟩	2.484(1) Å	
Δ	3.04×10^{-4}	Δ	15.3×10^{-4}	Δ	13.4×10^{-4}	
BVS	4.04(2)	BVS	3.05(1)	BVS	3.14(9)	
⟨Mn(1)−O⟩	1.916(2) Å	⟨Mn(2)−O⟩	1.948(3) Å	⟨Bi−O⟩	2.476(2) Å	12
Δ	4.4×10^{-4}	Δ	14.0×10^{-4}	Δ	14.2×10^{-4}	
BVS	3.88(4)	BVS	3.09(3)	BVS	3.21(7)	
⟨Mn(1)−O⟩	1.919(2) Å	⟨Mn(2)−O⟩	1.966(3) Å	⟨Bi−O⟩	2.468(2) Å	19
Δ	4.4×10^{-4}	Δ	14.0×10^{-4}	Δ	13.1×10^{-4}	
BVS	3.84(9)	BVS	3.10(7)	BVS	3.24(5)	
⟨Mn(1)−O⟩	1.912(2) Å	⟨Mn(2)−O⟩	1.95(4) Å	⟨Bi−O⟩	2.471(4) Å	20
Δ	2.7×10^{-4}	Δ	11.3×10^{-4}	Δ	13.0×10^{-4}	
BVS	3.91(8)	BVS	3.03(5)	BVS	3.23(6)	
⟨Mn(1)−O⟩	1.874 (1) Å	⟨Mn(2)−O⟩	1.953(1) Å	not reported		11
Δ	2.4×10^{-4}	Δ	6.0×10^{-4}			
BVS	4.36(3)	BVS	3.08(3)			

Table 3. Results of Determination of the Cationic Stoichiometry in $BiMn_2O_5$ Using ICP-OES[a]

atomic ratio	stoichiometry	sample A	sample B	sample C	sample D
Bi/Mn	0.5	0.46 ± 0.01	0.48 ± 0.01	0.47 ± 0.01	0.48 ± 0.01

[a] The errors bars are relative to the absolute weight mass errors (0.1 mg).

Table 4. A divergence from the linear domain characteristic of a paramagnetic regime occurs at one temperature about $|\theta_{CW}|$ far from the minimum corresponding to the Néel temperature. The Curie constant values are all higher than the ones expected from the ionic model with a stoichiometric composition $C(BiMn_2O_5) = 3 + 1.875 = 4.875$ cm^3·K/mol. Such an enhancement of the Curie constant or of its related effective paramagnetic moment is indeed commonly found in the literature. They can reach values from 5.2 to 5.9 cm^3·K/mol.[12]

Let us recall that such high values were already observed on Bi-doped calcium manganite perovskite and interpreted to be due to cluster intergrowth.[24] In the perovskite-like bismuth manganites, such clusters are believed to occur in the charge-ordering regime at temperatures below the ionic paramagnetic regime. In our study, it would be in the paramagnetic regime that cluster formation would take place in $BiMn_2O_5$ materials in relation to the given structural description. This would indicate an intrinsic charge-ordering model related to the crystallographic framework. However, our XRD and ICP-OES analyses point out a bismuth deficiency and our Mohr salt titration does not support a Mn^{3+}/Mn^{4+} ratio equal to 1. Instead, with $Mn^{3+} = 1.30 \pm 0.02$ and $Mn^{4+} = 0.70 \pm 0.04$ for samples B and C, a high Mn^{3+}/Mn^{4+} ratio close to 2 is estimated, giving the expected Curie constants $C(S_{B,C}) = 1.30 \times 3 + 0.70 \times 1.875 = 5.21$ cm^3·K/mol for both samples. The experimental values match unambiguously well with these expectations. Such a good agreement using an ionic model with a Mn^{3+}/Mn^{4+} ratio far from 1 suggests that the observed discrepancy in the Curie−Weiss constant (or in the effective paramagnetic moment) probably comes from the bismuth deficiency that enhanced the Mn^{3+} content. In the conclusion of our magnetic property studies, our results highlight a high experimental Curie constant

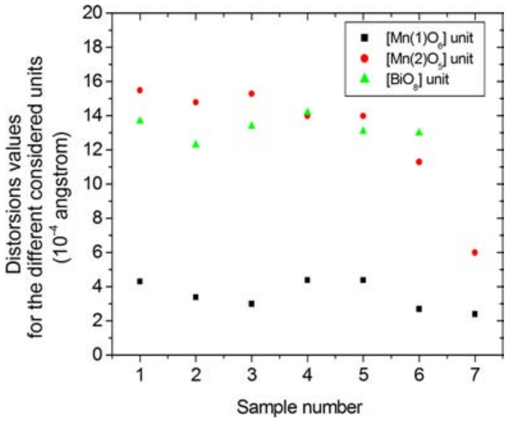

Figure 2. Synthesis and characterization dependence of the relevant distortion of the $[Mn(1)O_6]$, $[Mn(2)O_5]$, and $[BiO_8]$ units from eq 1 in comparison with the literature. Sample numbers 1−3 are related to samples A−C from our study, sample number 4 is related to ref 12, sample number 5 is related to ref 19, sample number 6 is related to ref 20, and sample number 7 is related to ref 11.

Table 4. Néel Temperature Depending on the Synthesis Method with the Parameters Obtained after the Curie−Weiss Law Fitting

sample	C (cm^3·K/mol)	θ_{CW} (K)	T_N (K)	$\|\theta_{CW}/T_N\|$
A	5.2	−247	33 ± 2	7.5
B	5.1	−243	37 ± 2	6.6
C	5.4	−262	39 ± 2	6.7

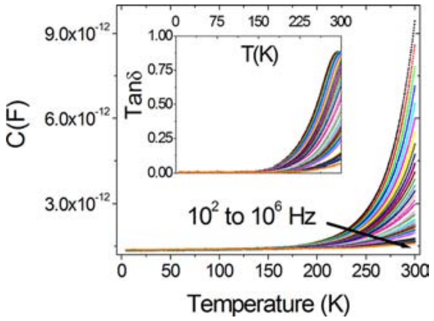

Figure 4. Evolution of the capacitance and dielectric loss (tan δ) versus temperature and frequency ranging from 10^2 to 10^6 Hz.

originating from an ionic model with a large excess of Mn^{3+} with respect to the Mn^{4+} content.

Considering that (i) all of our sintered $BiMn_2O_5$ phases are insulating (the room temperature resistances are R_{SB} = 2.1 × 10^8 Ω for sample B and R_{SC}= 3.5 × 10^9 Ω for sample C), the temperature dependence of their resistivities is then not measurable and (ii) nonclassical antiferromagnetic ordering could break the inversion symmetry of the nuclear structure, allowing for ferroelectricity,[1] we measured the temperature dependence of the dielectric properties of sample C. This sample has magnetic properties closer than the published ones that will allow us to discuss its multiferroic properties, as was previously proposed from first principles calculations.[25,26]

The dielectric properties were investigated in the temperature range 5−300 K on sample C and yielded reproducible results. As seen in Figure 4, neither a ferroelectric nor a relaxor transition was found in the probed temperature range. The dielectric losses increase drastically from 150 K and so does the capacitance, indicating the onset of a conduction mechanism. Interestingly, this onset coincides with the onset of the paramagnetic regime and is likely consistent with a hopping mechanism. It should be noted that the dielectric losses are extremely small below 150 K, confirming the good insulating properties for this sample in this temperature range. Given that the sample is insulating at room temperature and has an oxygen deficiency, this hopping mechanism certainly originates from oxygen vacancies, as suggested by Lin and co-workers.[15]

As mentioned above for the magnetic susceptibility, the deviation of the Curie−Weiss law is far from the Néel temperature for our samples. This scenario was proposed to be related to the appearance of magnetic correlations through the spin−phonon coupling mechanism.[27] We have then carried out specific heat measurements on sample C in a large range of temperatures to estimate the total magnetic contribution to the specific heat and its relative contribution at the Néel temperature.

In Figure 5a, the temperature dependence of the specific heat for sample C clearly shows an abrupt upturn at T = 39.5 ± 0.5 K when the temperature decreases. This is in agreement with the antiferromagnetic ordering observed on the magnetic susceptibility. Because we did not observe any dielectric transition and there is no reported structural transition either from the neutron diffraction study[12] or from the synchrotron XRD study,[19] we assumed a purely magnetic contribution for

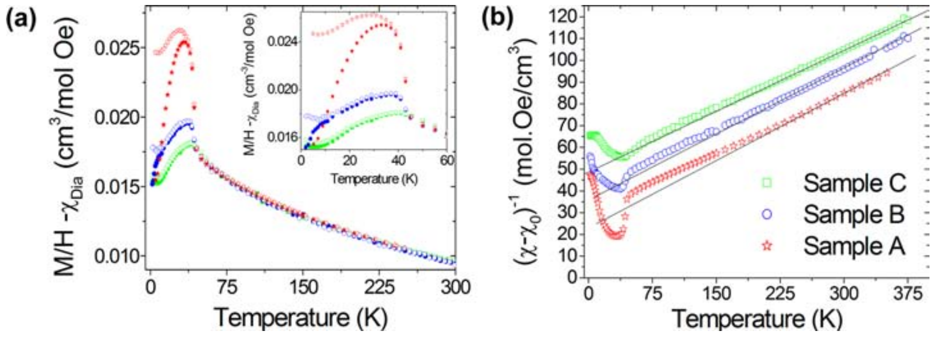

Figure 3. (a) Thermal evolution of the dc magnetic susceptibility in ZFC (closed symbols) and FC (open symbols) conditions for samples A (red stars), B (blue circles), and C (green squares) after subtraction of a small diamagnetic constant term (see the text). The inset shows the enlarged magnetic transition. (b) Corresponding T dependence of the inverse of the dc magnetic susceptibility. For samples B (middle) and A (bottom), they were vertically translated as −10 and −20 mol·Oe/cm^3, respectively, for better visualization. The solid lines represent extrapolations of the Curie−Weiss behavior that match the data for T > 250 K.

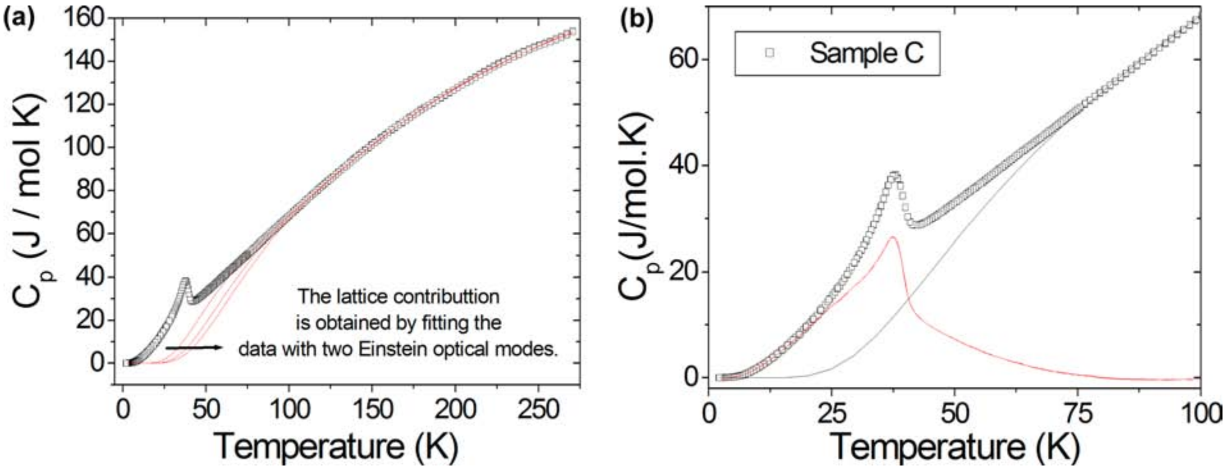

Figure 5. (a) Temperature dependence of the specific heat. The solid lines represent the calculated lattice contributions with different temperature ranges starting from 75 K (left) to 125 K (right). (b) Thermal evolution of the magnetic contribution to the specific heat, the phonon contribution extracted in the 100−270 K temperature range, and the total specific heat.

Table 5. Summary of the Fitting Results of the Specific Heat Measurement on Sample C Using the Einstein Model[a]

	Einstein model					
	normalized weighted parameters		optical mode			
temperature range (K) used to refine the phonon contribution	a_1	a_2	T_E^1 (K)	T_E^2 (K)	fit quality χ^2	magnetic entropy (J/mol·K) associated with the magnetic transition
75−270	0.44	0.58	203	682	0.1	19.4
100−270	0.53	0.52	247	768	0.05	25.5
125−270	0.59	0.47	276	832	0.06	29.6
150−270	physically incoherent at low temperature					

[a] Different ranges of temperatures and associated magnetic entropies were considered as indicated.

the peak on the specific heat. To extract the magnetic contribution from the total specific heat, the phonon contribution was fitted as follows. An Einstein model was used in the different range of temperatures following the fit quality factor. The starting Einstein temperatures were selected based on the intense optical mode observed from Raman spectroscopy.[27] The fit results are shown in Table 5. It turned out that the use of more than two optical models was not necessary. They can be associated with the oscillation of Bi and Mn atoms for the lowest Einstein temperature and with the oscillation of O atoms for the highest Einstein temperature.[12] The magnetic entropy can be determined through the integral of the magnetic contribution of the specific heat $\Delta S_M(T,H) = \int_0^T (C_{mag}/T)\ \partial T$. From our analysis, three different magnetic contributions were calculated depending on the range of temperatures, i.e., from 2 to 75 K, from 2 to 100 K, and from 2 to 125 K, giving ΔS_M = 19.4, 25.5, and 29.6 kJ/mol, respectively. Those magnetic entropy changes need to be compared with the expected value of free Mn^{3+} and Mn^{4+} for a stoichiometric material, $\Delta S_{mag} = R\ \ln[2S(Mn^{3+}) + 1] + R\ \ln[2S(Mn^{4+}) + 1] = 24.9$ J/mol·K, and for a more appropriate Mn^{3+} and Mn^{4+} ion distribution found for sample C, $\Delta S_{mag} = 1.30R\ \ln[2S(Mn^{3+}) + 1] + 0.70R\ \ln[2S(Mn^{4+}) + 1] = 25.4$ J/mol·K. When integration of the magnetic specific heat is performed up to 100 K to account for the total magnetic entropy, it perfectly matches with the expected values. This demonstrates that a short-range ordering occurs at temperatures far from the long-range antiferromagnetic ordering temperature T_N. Finally, the shape and particularly the low-temperature asymmetry of the magnetic contribution suggest that a long-range-ordering magnetic transition is indeed achieved following a complex phenomenon that is also indicated by the upturn of the magnetic susceptibility in FCC mode around 8 K (inset, Figure 3a).

■ DISCUSSION

First, it is important to underline the coherence between our collected data and the published data: (i) the amplitude of our magnetic susceptibility is on the same order of magnitude as those published;[12,19] (ii) the mean-square relative deviations calculated from the average bond length in the three different crystallographic units are consistent with the literature, as seen in Figure 2; (iii) a hopping mechanism originating from oxygen vacancies can interpret our temperature dependence of the capacitance and dielectric loss, as was already proposed.[15] These coherences of measurement unambiguously suggest that the physical and chemical properties of our samples A−C are very close to those prepared under different conditions.

In addition, we remind everyone that the Bi 6s lone pair breaks the crystal inversion symmetry to induce the ferroelectric properties in $BiMnO_3$[28] or $BiFeO_3$.[29] In contrast, in RMn_2O_5 materials, magnetoelastic and/or magnetoelectronic interactions are taken into account to induce such properties. They are not related to any structural transition but would result either from a spiral spin order or from antisymmetric exchange-striction effects in a fully charge-ordered structure, where Mn^{3+} and Mn^{4+} ions are located on two different crystallographic sites.[30] Both models are supported by an incommensurable magnetic ordering. Further reported by Blake and co-workers,[31] the radius of R would determine the sign of the magnetic exchange between adjacent planes in RMn_2O_5 and subsequently the noncollinearity of the spins in the *ab* plane.

Let us first consider the crystallographic data of the $[Mn(1)O_6]$ and $[Mn(2)O_5]$ units, which are the basic blocks

Table 6. Average Interatomic Distances, Bond Valence Sum Calculation from Equation 1 Using All the Metal−Oxygen Bonding, and Distortion Relevant of the $[Mn(1)O_6]$, $[Mn(2)O_5]$, and $[RO_8]$ Units in Comparison with the Literature

$[Mn(1)O_6]$		$[Mn(2)O_5]$		$[RO_8]$		ref
⟨Mn(1)−O⟩	1.901(1) Å	⟨Mn(2)−O⟩	1.933(1) Å	not reported		Tb 31
Δ	1.8×10^{-4}	Δ	4.5×10^{-4}			
BVS	4.03(1)	BVS	3.15(1)			
⟨Mn(1)−O⟩	1.899(1) Å	⟨Mn(2)−O⟩	1.931(1) Å	not reported		Ho 31
Δ	1.8×10^{-4}	Δ	4.5×10^{-4}			
BVS	4.05(1)	BVS	3.17(1)			
⟨Mn(1)−O⟩	1.905(1) Å	⟨Mn(2)−O⟩	1.919(1) Å	not reported		Dy 31
Δ	1.4×10^{-4}	Δ	8.0×10^{-4}			
BVS	3.99(1)	BVS	3.28(1)			
⟨Mn(1)−O⟩	1.904(27) Å	⟨Mn(2)−O⟩	1.957(29) Å	⟨La−O⟩	2.509(27) Å	La 7
Δ	2.9×10^{-4}	Δ	23.2×10^{-4}	Δ	2.1×10^{-4}	
BVS	4.0(0)	BVS	3.02(5)	BVS	3.25(8)	
⟨Mn(1)−O⟩	1.907(31) Å	⟨Mn(2)−O⟩	1.932(31) Å	⟨Nd−O⟩	2.467(31) Å	Nd 7
Δ	4.0×10^{-4}	Δ	10.5×10^{-4}	Δ	1.5×10^{-4}	
BVS	3.97(4)	BVS	3.18(6)	BVS	3.03(8)	
⟨Mn(1)−O⟩	1.902(3) Å	⟨Mn(2)−O⟩	1.938(4) Å	⟨Ho−O⟩	2.382(1) Å	Ho 20
Δ	2.0×10^{-4}	Δ	4.8×10^{-4}	Δ	2.0×10^{-4}	
BVS	4.02(2)	BVS	3.11(1)	BVS	3.08(5)	

for building up the crystallographic framework. The calculated average distances are quite different with $d_{\langle Mn(1)-O\rangle}$= 1.90 Å for the octahedral site and $d_{\langle Mn(2)-O\rangle}$= 1.95 Å for the pyramidal site. There is such a clear difference on the bond distances and consequently on the BVS calculations[32] that a charge-ordering model is proposed in the $BiMn_2O_5$ material, with Mn^{4+} located within the octahedral environment (shorter distance and distortion) and Mn^{3+} located within the squared-based pyramid (larger distance and distortion) in favor of the Jahn−Teller effect. However, if the discussion is extended to all of the RMn_2O_5 materials (see Tables 2 and 6), the peculiarity between the materials known to exhibit ferroelectric properties with R = Tb, Ho, and Dy[4,33] and the others with R = La, Nd, and Bi is not straightforward. Still, whatever R is, the separation on two ionic sites is valid. That is why it is further supported by the characterizations of sample C, i.e., (i) chemical analysis showing that both oxygen and bismuth are understoichiometric and (ii) the absence of any ferroelectric state, we suggest that an ionic Mn^{3+} and Mn^{4+} charge ordering is likely not the driving force for ferroelectric properties. Then, the plot in Figure 6 is the mean-square relative deviations Δ from the average bond length of the three different $[Mn(1)O_6]$, $[Mn(2)O_5]$, and $[RO_8]$ units versus the *R* ionic radius. Our analysis shows two interesting trends. The first one is that the Δ values for the $[Mn(2)O_5]$ unit are more significant on the nonferroelectric compounds than on the ferroelectric ones. It turns out that any large distortion of the $[Mn(2)O_5]$ units would preclude any ferroelectric properties. Second, the Δ values for the $[RO_8]$ (R = La, Nd, Ho) units are on the same order of magnitude but much smaller than the ones found for the $[BiO_8]$ polyhedron. The observed large distortion of the $[BiO_8]$ polyhedron is enhanced by the $6s^2$ lone pair of the Bi^{3+} cation, but it does not lead to any breaking of the inversion symmetry.

Regarding the magnetic properties, a magnetic characteristic temperature was underlined and called *T** in relation to an anomalous phonon shift on temperature-dependent Raman scattering.[27] *T** is consistent with the temperatures for which a clear deviation of the linear thermal expansion coefficient starts[19] and a local peak on the pyroelectric coefficient is observed.[16] Besides, a clear maximum on the temperature derivative of the inverse magnetic susceptibility was considered to estimate *T**[27], as indicated in Figure 7a. It is not yet clearly defined for samples A and B because magnetic transitions show an abrupt character, but such a derivative on sample C gives *T** equal to 58 ± 2 K. However, sample C can no longer be considered as a dielectric, and thus no ferroelectric or relaxor behavior can be probed or envisaged. It is worth mentioning that, although a relaxor behavior at high temperature is claimed in the study of Fier et al.,[16] their measured dielectric losses are actually around 2 orders of magnitude larger than those in our data around room temperature.

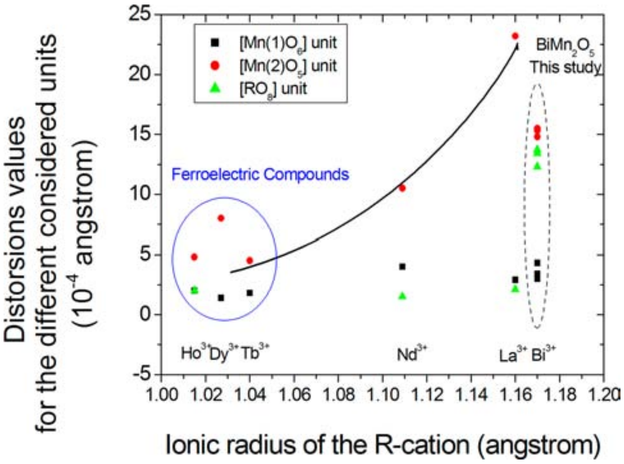

Figure 6. Ionic radius of the *R* cation as a function of the average distortion of the different polyhedral units. Dashed and solid lines are guides for the eyes.

Second, the deviation of the Curie−Weiss law in the inverse magnetic susceptibility versus temperature curves occurs at a temperature close to the absolute value of the Curie−Weiss temperature θ_{CW}. A short-range-ordering domain is unambiguously shown at a temperature well above the long-range-ordering temperature T_N in line with our specific heat analysis. Besides, the ratio $|\theta_{CW}|/T_N$ shown in Table 4 could signify some magnetic frustration phenomenon. It suggests a complex

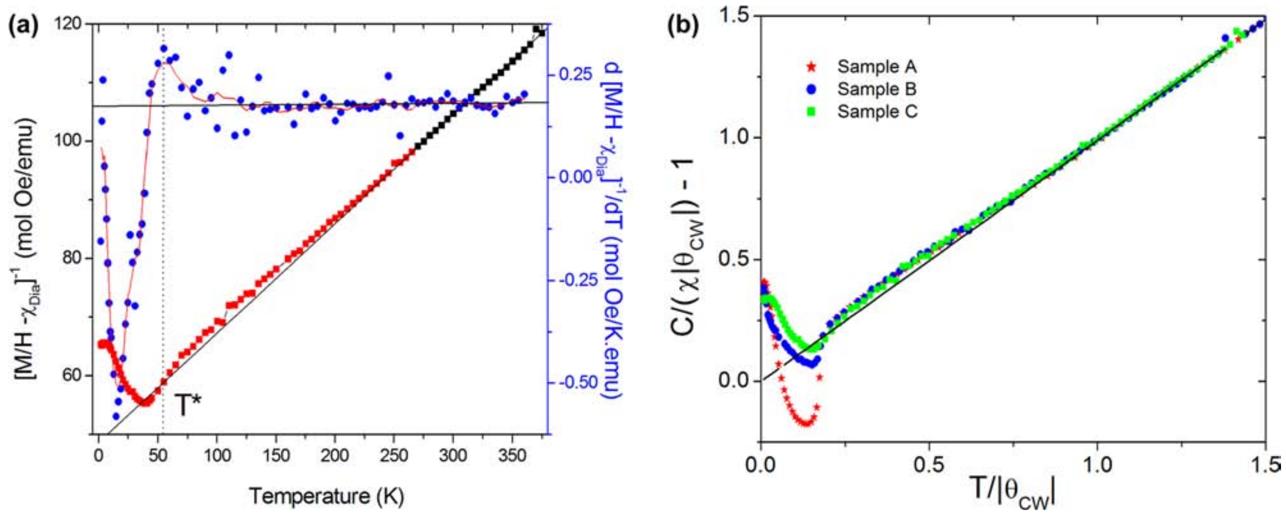

Figure 7. (Left) Temperature dependence of the inverse of the dc magnetic susceptibility for sample C (left scale) and its temperature-derivative (right scale). (Right) Scaled inverse susceptibility as a function of the scaled temperature as described by the formula (2). The solid line represents ideal Curie–Weiss paramagnetism obtained by fitting the data when $T/|\theta_{CW}| > 1$ for sample B.

magnetic ground state in the form of magnetic frustration[12] with strong magnetic correlations starting at a temperature close to $|\theta_{CW}|$ and significantly far from T_N and T^*. To better characterize it, we plot Figure 7b following the approach proposed by Melot and co-workers.[34] The scaled inverse susceptibility as a function of the scaled temperature is described by the following formula:

$$\frac{C}{\chi \times \theta_{CW}} = \frac{T}{\theta_{CW}} - 1 \tag{2}$$

The fit of the scaled inverse susceptibilities with a fixed slope equal to 1 within the ideal Curie–Weiss behavior range of temperature is suitable only if the scaled temperature $T/|\theta_{CW}| > 1$. They give straight lines through zero (−0.0108 ± 0.0014 for sample A, −0.011 ± 0.001 for sample B, and −0.0072 ± 0.0015 for sample C). When the scaled temperature decreases, a positive deviation from the ideal Curie–Weiss behavior is highlighted, indicating the presence of compensated antiferromagnetic interaction within the scaled temperature range [0.185, 1] for samples A and B and [0.209, 1] for sample C. They correspond to 45–245 and 58–263 K temperature ranges, respectively. When the scaled temperature further decreases, the deviation changes to negative signs, indicating uncompensated antiferromagnetism (ferrimagnetism). Interestingly, the deviation change their signs when the temperature reaches T^*, as shown from the analysis of sample C. A change of the sign of the deviation from the ideal paramagnet behavior was already observed on the $LiFeSO_4F$ material for which intrachain and interchain interactions were considered to compete.[35] In our sample, the nearest-neighbor Mn–O–Mn superexchange interactions continuously change following the considered Mn^{4+}/Mn^{3+} ratio in relation with the bismuth and/or oxygen deficiencies. Combined with the large distortion of the [Mn(2)O_5] unit linked to the lone pair of the Bi^{3+} cation, it would preclude determination of a finite sign of the magnetic exchange between adjacent planes in RMn_2O_5. The intraplane and interplane magnetic interactions could not simultaneously be satisfied, resulting in the proposed frustrated-spin configuration.[12] In contrast with the RMn_2O_5 materials showing ferroelectric properties,[12] we suggest that the commensurate magnetic structure below 39 K for $BiMn_2O_5$ materials would be linked to a random distribution of the noncollinear spins in the *ab* plane due to distorsions induced by the Bi^{3+} lone pair. Such an analysis would suggest that long-range spiral spin order would be the ferroelectric driving force. Finally, we assume that T^* is an intrinsic characteristic temperature for $BiMn_2O_5$ phases because it gives the temperature where the deviation from an ideal Curie–Weiss paramagnet changes in sign. However, T^* is not in relation to any ferroelectric properties.

■ CONCLUSION

We investigated a series of $BiMn_2O_5$ materials prepared by sealed-tube synthesis. The Rietveld refinement at room temperature using the initial structure model given by Alonso and co-workers[7] led to the bismuth deficiency values in accordance with ICP-OES analysis. It indicates that the crystallographic structure is unambiguously stable even if the ratio Mn^{3+}/Mn^{4+} is not equal to 1. Further supportive information is given by the Mohr salt titration and the Curie–Weiss law analysis of the magnetic susceptibility measurement. Concerning the multiferroic properties, the specific heat and scaled magnetic susceptibility analysis confirm that the antiferromagnetic short-range character occurring at $|\theta_{CW}|$ far from the Néel temperature is intrinsic. Another magnetic characteristic temperature T^* is an intrinsic and would indicate a compensated-to-uncompensated antiferromagnetic interaction transition. T^* values fluctuate around 50 ± 5 K because the transition is linked to the bismuth and oxygen soichiometries. However, T^* does not mark any ferroelectric behavior. Indeed, the frequency dependence of the dielectric loss peak occurring around room temperature is assumed to be due to an electronic hopping mechanism arising from oxygen vacancies.

In contrast with the mean-square relative deviations Δ found for the [Mn(2)O_5] unit in ferroelectric RMn_2O_5 materials, a large Δ is shown in $BiMn_2O_5$ materials. It is certainly in relation to the Bi^{3+} lone-pair effect, but it excludes any ferroelectric properties. Further, while in a half-doped manganite perovskite-type structure the charge-ordering phenomenon is correlated to the appearance of superstructure peaks,[36] the question arising from our work is their observation on ferroelectric RMn_2O_5 compounds in comparison to the nonferroelectric ones. Our analysis thus better suggests that long-range spiral spin order would be the ferroelectric driving force.

■ ASSOCIATED CONTENT

Ⓢ Supporting Information

XRD patterns $BiMn_2O_5$ for samples A–D and table of cell parameters, structural parameters, and relative cationic occupancies. This material is available free of charge via the Internet at http://pubs.acs.org.

■ AUTHOR INFORMATION

Corresponding Author

*E-mail: toulemonde@icmcb-bordeaux.cnrs.fr.

Notes

The authors declare no competing financial interest.

■ ACKNOWLEDGMENTS

R. Decourt (for C_p measurements), E. Lebraud (for XRD data collection), S. Pechev (for XRD analysis), J. Villot (for sealed-tube synthesis), and L. Etienne (for ICP-OES analysis) are thanked for their technical support. This work has been supported by the European project "SOPRANO" under Marie Curie actions (Grant PITNGA-2008-214040).

■ REFERENCES

(1) Tokura, Y.; Seki, S. *Adv. Mater.* **2010**, *22*, 1554.

(2) Kenzelmann, R. M.; Harris, A. B.; Jonas, S.; Broholm, C.; Schefer, J.; Kim, S. B.; Zhang, C. L.; Cheong, S.-W.; Vajk, O. P.; Lynn, J. W. *Phys. Rev. Lett.* **2005**, *95*, 087206.

(3) Ikeda, N.; Ohsumi, H.; Ohwada, K.; Ishii, K.; Inami, T.; Kakurai, K.; Murakami, Y.; Yoshii, K.; Mori, S.; Horibe, Y.; Kitô, H. *Nature* **2005**, *436*, 1136.

(4) Hur, N.; Park, S.; Sharma, P. A.; Ahn, J.; Guha, S.; Cheong, S.-W. *Nature* **2004**, *429*, 392.

(5) Quezel-Ambrunaz, S.; Bertaut, E. F.; Buisson., G. *C. R. Acad. Sci.* **1964**, *258*, 3025.

(6) Bertaut, E. F.; Buisson, G.; Durif, A.; Mareschal, A.; Montmory, M. C.; Quezel-Ambrunaz., S. *Bull. Soc. Chim. Fr.* **1965**, 1132.

(7) Alonso, J. A.; Casais, M. T.; Martínez-Lope, M. J.; Rasines., I. *J. Solid State Chem.* **1997**, *129*, 105.

(8) Retuerto, M.; Martinez-Lope, M. J.; Krezhov, K.; Fernandez-Diaz, M. T.; Alonso, J. A. *J. Solid State Chem.* **2011**, *184*, 2428.

(9) Muñoz, A.; Alonso, J. A.; Martínez-Lope, M. J.; Martínez, J. L. *Chem. Mater.* **2004**, *16*, 4087.

(10) Giaquinta, D. M.; zur Loye, H. C. *J. Alloys Compd.* **1992**, *184*, 151.

(11) Nguyen, N.; Legrain, M.; Ducouret, A.; Raveau, B. *J. Mater. Chem.* **1999**, *9*, 73.

(12) Munoz, A.; Alonso, J. A.; Casais, M. T.; Martinez-Lope, M. J.; Martinez, J. L.; Fernandez-Diaz, M. T. *Phys. Rev. B* **2002**, *65*, 144423.

(13) Jia, R.-J.; Han, J.-T.; Wu, X.-J.; Wu, C.-L.; Huang, Y.-H.; Huang, W. *Mater. Res. Bull.* **2008**, *43*, 1702.

(14) Saravana Kumar, K.; Venkateswaran, C. *J. Phys. D: Appl. Phys.* **2011**, *44*, 3250001.

(15) Lin, Y. Q.; Wu, Y. J.; Chen, X. M.; Gu, S. P.; Tong, J.; Guan, S. *J. Appl. Phys.* **2009**, *105*, 054109.

(16) Fier, I.; Walmsley, L.; Souza, J. A. *J. Appl. Phys.* **2001**, *110*, 084101.

(17) Rodriguez-Carvajal, J. *Physica B* **1993**, *192*, 55.

(18) Toulemonde, O.; Abel, J.; Ying, C.; Wattiaux, A .; Gaudin, E. *Chem. Mater.* **2012**, *24*, 1128.

(19) Granado, E.; Eleotério, M. S.; García-Flores, A. F.; Souza, J. A.; Golovenchits, E. I.; Sanina, V. A. *Phys. Rev. B* **2008**, *77*, 134101.

(20) Grzechnik, A.; Tolkiehn, M.; Morgenroth, W.; Friese, K. *J. Phys.: Condens. Matter* **2010**, *22*, 275401.

(21) Brown, I. D.; Shanon, R. D. *Acta Crystallogr.* **1973**, *A29*, 266.

(22) Topfer, J.; Goodenough, J. B. *J. Solid State Chem.* **1997**, *130*, 117.

(23) Chen, Y.; Yuan, H.; Tian, G.; Zhang, G.; Feng, S. *J. Solid State Chem.* **2007**, *180*, 1340.

(24) Toulemonde, O.; Skovsen, I.; Mesguich, F.; Gaudin, E. *Solid State Sci.* **2008**, *10*, 476e480.

(25) Zhang, J.; Xu, B.; Li, X. F.; Yao, K. L.; Liu, Z. L. *J. Magn. Magn. Mater.* **2011**, *323*, 1599.

(26) Li, N.; Yao, K.; Gao, G.; Sun, Z.; Li, L. *Phys. Chem. Chem. Phys.* **2011**, *13*, 9418.

(27) García-Flores, A. F.; Granado, E.; Martinho, H.; Urbano, R. R.; Rettori, C.; Golovenchits, E. I.; Sanina, V. A.; Oseroff, S. B.; Park, S.; Cheong, S.-W. *Phys. Rev. B* **2006**, *73*, 104411.

(28) Kimura, T.; Kawamoto, S.; Yamada, I.; Azuma, M.; Takano, M.; Tokura, Y. *Phys. Rev. B* **2003**, *67*, 180401R.

(29) Fischer, P.; Polomska, M.; Sosnowska, I.; Szymanski, M. *J. Phys. C: Solid State Phys.* **1980**, *13*, 1931.

(30) Radaelli, P. G.; Chapon, L. C. *J. Phys.: Condens. Matter* **2008**, *20*, 434213.

(31) Blake, G. R.; Chapon, L. C.; Radaelli, P. G.; Park, S.; Hur, N.; Cheong, S.-W.; Rodríguez-Carvajal, J. *Phys. Rev. B* **2005**, *71*, 214402.

(32) Brown, I. D.; Altermatt, D. *Acta Crystallogr.* **1985**, *B41*, 244.

(33) Hur, N.; Park, S.; Sharma, P. A.; Guha, S.; Cheong, S.-W. *Phys. Rev. Lett.* **2004**, *93*, 107207.

(34) Melot, B. C.; Drewes, J. E.; Seshadri, R.; Stoudenmire, E. M.; Ramirez, A. P. *J. Phys.: Condens. Matter* **2009**, *21*, 216007.

(35) Melot, B. C.; Rousse, G.; Chotard, J.-N.; Ati, M.; Rodríguez-Carvajal, J.; Kemei, M. C.; Tarascon, J.-M. *Chem. Mater.* **2011**, *23*, 2922.

(36) Chen, C. T.; Cheong, S.-W. *Phys. Rev. Lett.* **1996**, *76*, 4042.